PNAS RESEARCH ARTICLE | APPLIED PHYSICAL SCIENCES

Anomalous grain dynamics and grain locomotion of odd crystals

Zhi-Feng Huang[a,1], Michael te Vrugt[b,1], Raphael Wittkowski[c,d,1], and Hartmut Löwen[e,1]

Affiliations are included on p. 11.

Edited by Suraj Shankar, University of Michigan, Ann Arbor, MI; received May 6, 2025; accepted September 6, 2025 by Editorial Board Member Mehran Kardar

Crystalline or polycrystalline systems governed by odd elastic responses are known to exhibit complex dynamical behaviors involving self-propelled dynamics of topological defects with spontaneous self-rotation of chiral crystallites. Unveiling and controlling the underlying mechanisms require studies across multiple scales. We develop such a type of approach that bridges between microscopic and mesoscopic scales, in the form of a phase field crystal model incorporating transverse interactions. This continuum density field theory features two-dimensional parity symmetry breaking and odd elasticity, and generates a variety of interesting phenomena that agree well with recent experiments and particle-based simulations of active and living chiral crystals, including self-rotating crystallites, dislocation self-propulsion and proliferation, and fragmentation in polycrystals. We identify a distinct type of surface cusp instability induced by self-generated surface odd stress that results in self-fission of single-crystalline grains. This mechanism is pivotal for the occurrence of various anomalous grain dynamics for odd crystals, particularly the predictions of a transition from normal to reverse Ostwald ripening for self-rotating odd grains, and a transition from grain coarsening to grain self-fragmentation in the dynamical polycrystalline state with an increase of transverse interaction strength. We also demonstrate that the single-grain dynamics can be maneuvered through the variation of interparticle transverse interactions. This allows to steer the desired pathway of grain locomotion and to control the transition between grain self-rotation, self-rolling, and self-translation. Our results provide insights for the design and control of structural and dynamical properties of active odd elastic materials.

odd elasticity | nonreciprocity | two-dimensional chirality | grain dynamics | phase field crystal

Significance

Odd crystals with transverse interactions arise in a broad variety of experimental setups, ranging from starfish embryos to magnetic colloids. In these systems, a wealth of notable effects such as spontaneous self-rotation and recurrent self-fragmentation of crystallites have been discovered. In this work, we present a continuum field model bridging microscopic and mesoscopic scales that allows to uncover the mechanism underlying these phenomena, namely a surface cusp instability resulting from self-generated odd stresses and the subsequent grain self-fission. We also use the model to develop a way of controlling the dynamics of odd systems, which allows, e.g., for steering the locomotion of odd elastic grains to achieve self-transport.

The understanding and control of grain growth dynamics are among the key subjects in the study of crystalline and polycrystalline materials. Typical phenomena include the classical process of Ostwald ripening (1), which corresponds to the growth of larger grains at the expense of vanishing smaller ones via intergrain particle diffusion through the liquid medium, and the dynamics of grain coarsening in polycrystals, for which the evolution of topological defects, particularly grain boundaries and dislocations, plays a crucial role (2, 3). Most of the conventional passive materials are potential systems, where microscopically the interparticle interactions are governed by center–center longitudinal forces and the corresponding interaction potentials, while mesoscopically and macroscopically, the system evolution and grain dynamics are driven by the pathways toward the equilibrium state characterized by minimum free energy of the system. However, this principle of thermodynamic-potential minimization can no longer be applied for active systems, particularly when the microscopic interactions involve nonconservative transverse forces oriented perpendicularly to the center–center direction of the two interacting active bodies [as originating from, e.g., hydrodynamic near-field interactions between spinning particles (4–8)]. This can lead to the existence of nonreciprocal torques between two active particles; the resulting many-body systems are nonpotential and intrinsically nonequilibrium.

Although in the bulk state of a perfect crystalline lattice, all the interparticle transverse forces are balanced and do not affect the crystal stability, small deformations will lead to odd elastic responses, as identified in continuum odd elasticity theory (9), with antisymmetric or odd elastic constant tensor $C^{(\mathrm{o})}_{ijkl} = -C^{(\mathrm{o})}_{klij}$ and asymmetric stress $\sigma_{ij} \neq \sigma_{ji}$ showing nonzero internal torque caused by transverse forces and the lack of angular momentum conservation. This results in self-generated dynamics of topological defects inside crystalline grains and the self-rotation of odd crystallites induced by nonzero net odd stress and torque on surface, as observed in both experiments (6–8) and simulations

Author contributions: Z.-F.H., M.t.V., R.W., and H.L. designed research; Z.-F.H. and M.t.V. performed research; Z.-F.H. analyzed data; and Z.-F.H., M.t.V., R.W., and H.L. wrote the paper.

The authors declare no competing interest.

This article is a PNAS Direct Submission. S.S. is a guest editor invited by the Editorial Board.

Copyright © 2025 the Author(s). Published by PNAS. This article is distributed under Creative Commons Attribution-NonCommercial-NoDerivatives License 4.0 (CC BY-NC-ND).

[1]To whom correspondence may be addressed. Email: huang@wayne.edu, tevrugtm@uni-mainz.de, rgwitt25@dwi.rwth-aachen.de, or hlowen@hhu.de.

This article contains supporting information online at https://www.pnas.org/lookup/suppl/doi:10.1073/pnas.2511350122/-/DCSupplemental.

Published October 17, 2025.

Downloaded from https://www.pnas.org by UNIVERSITAETS DUESSELDORF on October 20, 2025 from IP address 134.99.64.130.

(6–8, 10–12) of various active and living chiral crystals formed by, e.g., swimming bacteria (6), starfish embryos (7), and magnetic colloids (8). More complex behaviors occur for large-scale odd polygrain systems activated by persistent dynamics of motile defects, such as the self-kneading polycrystal whorl state found in recent magnetic colloidal experiments (8).

Such chiral odd crystalline systems naturally involve multiple spatial and temporal scales that mutually couple, in particular microscopic scales at the individual particle or discrete-lattice level and mesoscopic scales of structural patterns or interfacial profiles across, e.g., solid–liquid or grain boundaries. However, current theoretical and computational studies of odd elastic systems mostly focus on two ends of the scaling spectrum, i.e., discrete particle-based simulations (6–8, 10–14), by which only limited length and time scales can be accessed, and continuum elasticity theory (9, 10, 15) for the description of long-wavelength behaviors of the system but with the absence of microscopic crystalline symmetry and structures. Although continuum field theories have been developed for the study of nonreciprocal active matter, including nonreciprocal coupling between different species (16–21) and nonreciprocal interactions within a single species (22, 23), what has been still lacking is a truly multiscale approach which incorporates the coupling and bridging between microscopic/discrete and mesoscopic/continuum scales for the modeling of odd crystalline or polycrystalline systems. This hinders our efforts on further examining and predicting the complex dynamical behavior of odd grains with elastic or plastic deformations.

Here, we develop such a micro- and mesoscale approach based on the phase field crystal (PFC) method, which incorporates discrete crystalline structure into continuum density field theory and well captures the system elasticity, plasticity, and multigrain dynamics (24–30), as has been demonstrated through its wide range of applications in solid, soft, and active systems (31–41). Effects of transverse interactions are introduced into this continuum field model as nonpotential contributions through derivation from microscopic particle dynamics, leading to a PFC model incorporating transverse interactions (T-PFC model) and the corresponding mesoscale amplitude equation formulation. The modeling reveals a number of intriguing properties of two-dimensional (2D) odd elastic crystals and grains involving complex dynamics of topological defects, with the underlying mechanisms elucidated via the development of a distinct type of surface cusp instability that leads to grain self-fission through dislocation proliferation. The model predictions also include three types of transitions for odd grain dynamics, namely a transition from normal to reverse Ostwald ripening, a transition between the traditional behavior of grain coarsening and the persistent grain self-fragmentation in the dynamical polycrystalline state, and in terms of grain locomotion, the controlled transition from self-rotation to self-rolling (a combination of self-rotation and translation) and to self-translation of grains. Our results are not only consistent with existing experiments and particle-based or molecular dynamics (MD) simulations of various active and living chiral crystalline systems but also predict mechanisms and conditions that are applicable and extendable to the further study of chiral material systems with odd elastic response.

Model

Based on the PFC approach, we represent the spatiotemporal distribution of particles by a local particle density variation field $\psi(\mathbf{r}, t)$. Contributions from longitudinal interactions are described by the PFC free energy functional $F_{\mathrm{PFC}} = \int d\mathbf{r}\,\{\frac{1}{2}\psi[-\epsilon + (\nabla^2 + q_0^2)^2]\psi - \frac{1}{3}g\psi^3 + \frac{1}{4}\psi^4\}$. This represents a minimal model for crystal formation, which depending on its parameters produces either a homogeneous (liquid) or a spatially ordered (crystalline) phase (26, 31). The parameter ϵ is a temperature-like parameter that determines whether the system is above or below the freezing transition, and q_0 determines the periodicity of the crystalline phase. We here set $q_0 = 1$ after rescaling by choosing the lattice spacing of the crystalline phase as a length scale. From a statistical mechanics point of view, the rescaled model parameters ϵ and g can be expressed via the Fourier components of interparticle direct correlation functions (25, 42). Specifically, the first two quadratic terms in F_{PFC} are related to the two-point direct correlation function, with ϵ measuring the distance from the crystal melting point and the second gradient term giving the spatially periodic structure of characteristic lattice wave number q_0. The cubic and quartic terms can be viewed as those from a Landau expansion which, as combined with the quadratic terms, give rise to the first-order liquid–solid phase transition. They have also been shown to connect to the three-point direct correlation function in classical dynamical density functional theory (42). The corresponding flux is given by $\mathbf{J}_{\mathrm{PFC}} = -\nabla\mu_{\mathrm{PFC}} = -\nabla\delta F_{\mathrm{PFC}}/\delta\psi$, where μ_{PFC} is the chemical potential. The transition and coexistence between solid and liquid (homogeneous) states are determined by ϵ and the average density $\bar{\psi}_0$.

For the odd solid system studied here, we incorporate the nonpotential contribution by coarse-graining the microscopic equations of motion of particles interacting via a transverse force $\mathbf{F}^{\perp}_{ab} = f^{\perp}(\mathbf{r}_a, \mathbf{r}_b)\hat{\mathbf{r}}^{\perp}_{ab}$ between any two particles a and b, with $\hat{\mathbf{r}}^{\perp}_{ab} = \hat{\mathbf{z}} \times \hat{\mathbf{r}}_{ab}$, $\hat{\mathbf{z}}$ the out-of-plane unit vector, and $\hat{\mathbf{r}}_{ab} = (\mathbf{r}_a - \mathbf{r}_b)/|\mathbf{r}_a - \mathbf{r}_b|$. Details of the derivation are given in *SI Appendix*. The nonpotential flux is found to be

$$J_{\mathrm{T},i} = -\psi\left(\alpha_0 + \alpha_1\nabla^2 + \alpha_2\nabla^4\right)\epsilon_{ij}\partial_j\psi, \qquad [1]$$

where $i, j = x, y$, ϵ_{ij} is the 2D Levi-Civita symbol, and α_k ($k = 0, 1, 2$) are proportional to the strength of transverse interaction (with expressions determined by the specific form of the transverse force $f^{\perp}$). Here, the coefficients α_k are allowed to vary with space and/or time. The term proportional to α_1 is consistent with the one found in the chiral current of a different type of chiral active matter, namely circle swimmers (43).

The dynamics of the density field is then governed by $\partial\psi/\partial t = -\nabla\cdot\mathbf{J} = -\nabla\cdot(\mathbf{J}_{\mathrm{T}} + \mathbf{J}_{\mathrm{PFC}})$ with a diffusive timescale, giving the T-PFC model equation

$$\frac{\partial\psi}{\partial t} = \left[\nabla(\alpha_0\psi)\times\nabla\psi + \nabla(\alpha_1\psi)\times\nabla\nabla^2\psi + \nabla(\alpha_2\psi)\times\nabla\nabla^4\psi\right]_z + \nabla^2\frac{\delta F_{\mathrm{PFC}}}{\delta\psi}. \qquad [2]$$

For spatially and temporally constant coefficients α_k, the T-PFC Eq. **2** reduces to

$$\frac{\partial\psi}{\partial t} = \left[(\nabla\psi)\times\nabla\left(\alpha_1\nabla^2\psi + \alpha_2\nabla^4\psi\right)\right]_z + \nabla^2\left[-\epsilon\psi + \left(\nabla^2 + q_0^2\right)^2\psi - g\psi^2 + \psi^3\right]. \qquad [3]$$

The first term of Eq. **3**, originating from transverse interactions, breaks the 2D parity symmetry, which can then lead to 2D chirality. It is also antisymmetric with respect to the exchange

Downloaded from https://www.pnas.org by UNIVERSITAETS DUESSELDORF on October 20, 2025 from IP address 134.99.64.130.

of x and y, resulting in a non-Hermitian dynamical matrix for the elastodynamics of the displacement field, a characteristic of nonreciprocity (*SI Appendix*). In addition, it is straightforward to prove that this 2D T-PFC equation is rotationally invariant with respect to a rotation about the z axis, i.e., maintaining global rotational invariance in 2D, in addition to translational invariance.

Amplitude Expansion. The mesoscale description of the model is obtained from the corresponding amplitude expansion, i.e.,

$$\psi = \psi_0 + \sum_{j=1}^{3} A_j e^{i\mathbf{q}_j^0\cdot\mathbf{r}} + \text{c.c.}, \qquad [4]$$

where $\mathbf{q}_1^0 = \tilde{q}_0(-\frac{\sqrt{3}}{2}\hat{\mathbf{x}}-\frac{1}{2}\hat{\mathbf{y}})$, $\mathbf{q}_2^0 = \tilde{q}_0\hat{\mathbf{y}}$, and $\mathbf{q}_3^0 = \tilde{q}_0(\frac{\sqrt{3}}{2}\hat{\mathbf{x}}-\frac{1}{2}\hat{\mathbf{y}})$ are the basic wave vectors of a 2D hexagonal lattice, with $\hat{\mathbf{x}}$ and $\hat{\mathbf{y}}$ the unit vectors along the x and y directions respectively, and $\tilde{q}_0$ ($\sim q_0$) is the steady-state selected wave number. The 0th-mode average density field ψ_0 and the complex amplitude A_j ($j = 1, 2, 3$) vary at the mesoscopic "slow" scales. Substituting Eq. **4** into Eq. **3** and following the procedure of amplitude equation formulation (42, 44) by separating microscopic and mesoscopic scales, we get

$$\begin{aligned}\frac{\partial\psi_0}{\partial t} &= \left[(\boldsymbol{\nabla}\psi_0)\times\boldsymbol{\nabla}\left(\alpha_1\nabla^2\psi_0+\alpha_2\nabla^4\psi_0\right)\right]_z \\ &+\sum_j\left\{\left[\left(\boldsymbol{\nabla}+i\mathbf{q}_j^0\right)A_j\right]\times\left(\boldsymbol{\nabla}-i\mathbf{q}_j^0\right)\right\}_z \\ &\mathcal{L}_j^*\left(\alpha_1+\alpha_2\mathcal{L}_j^*\right)A_j^* + \text{c.c.} + \nabla^2\frac{\delta\mathcal{F}_{\text{PFC}}}{\delta\psi_0}, \qquad [5]\end{aligned}$$

$$\begin{aligned}\frac{\partial A_j}{\partial t} &= \left[(\boldsymbol{\nabla}\psi_0)\times\left(\boldsymbol{\nabla}+i\mathbf{q}_j^0\right)\right]_z\mathcal{L}_j\left(\alpha_1+\alpha_2\mathcal{L}_j\right)A_j \\ &+\left\{\left[\left(\boldsymbol{\nabla}+i\mathbf{q}_j^0\right)A_j\right]\times\boldsymbol{\nabla}\left(\alpha_1\nabla^2\psi_0+\alpha_2\nabla^4\psi_0\right)\right\}_z \\ &+\sum_{l\neq k\neq j}\left\{\left[\left(\boldsymbol{\nabla}-i\mathbf{q}_l^0\right)A_l^*\right]\times\left(\boldsymbol{\nabla}-i\mathbf{q}_k^0\right)\right\}_z \\ &\mathcal{L}_k^*\left(\alpha_1+\alpha_2\mathcal{L}_k^*\right)A_k^* - \tilde{q}_0^2\frac{\delta\mathcal{F}_{\text{PFC}}}{\delta A_j^*}, \qquad [6]\end{aligned}$$

where "$*$" denotes complex conjugate, $\mathcal{L}_j = \nabla^2 + 2i\mathbf{q}_j^0\cdot\boldsymbol{\nabla} - \tilde{q}_0^2$ and $\mathcal{F}_{\text{PFC}}[A_j, \psi_0]$ is the mesoscale effective free energy functional (*SI Appendix*).

One-Mode Approximation for the Bulk State. For a pristine crystalline phase of hexagonal symmetry, $\psi_0 = \bar{\psi}_0$ and $A_j = A_j^0$ ($j = 1, 2, 3$) are constant in the one-mode approximation. Thus, the contributions from transverse interaction terms vanish, as seen from Eqs. **5** and **6**, and the exact solution of the steady state is given by

$$\begin{aligned}A_j^0 = A_0 = \frac{1}{15}\Big\{&g-3\bar{\psi}_0 \\ &+\sqrt{(g-3\bar{\psi}_0)^2-15\left[-\epsilon+(\tilde{q}_0^2-q_0^2)^2+3\bar{\psi}_0^2-2g\bar{\psi}_0\right]}\Big\}. \qquad [7]\end{aligned}$$

This agrees with the result of the original PFC model without transverse interactions. The one-mode phase diagram for solid and liquid phases (26) is the same as well. This is consistent with the microscopic picture of a perfect crystalline bulk state where neighboring transverse forces cancel out and thus have a negligible effect on the system stability, unless there exist elastoplastic deformations or interfaces with varying structural amplitudes, as will be addressed below.

Odd Elasticity. For small elastic deformations, the phases of complex amplitudes vary at long wavelength as a result of a displacement field $\mathbf{u}$, giving $A_j \simeq A_j^0\exp(-i\mathbf{q}_j^0\cdot\mathbf{u})$, where $A_j^0 \simeq A_0$ in the steady state with $\psi_0 \simeq \bar{\psi}_0$. From the amplitude Eqs. **5** and **6**, we show in *SI Appendix* that the displacement field $u_{j=x,y}$ satisfies the elastodynamical equation (i.e., the overdamped Cauchy's equation of motion)

$$\Gamma\frac{\partial u_j}{\partial t} = \partial_i\sigma_{ij} = C_{ijkl}\partial_i\partial_k u_l, \qquad [8]$$

where Γ is the drag coefficient, C_{ijkl} represents the elastic constant tensor, and $\sigma_{ij} = C_{ijkl}\partial_k u_l$ is the stress tensor. To the lowest order,

$$\begin{aligned}C_{1111} &= C_{2222} = \Gamma\tilde{q}_0^2\left(5\tilde{q}_0^2-2q_0^2\right), \\ C_{1122} &= C_{2211} = \Gamma\tilde{q}_0^2\left(2q_0^2-\tilde{q}_0^2\right), \\ C_{1212} &= C_{2121} = C_{1221} = C_{2112} = \Gamma\tilde{q}_0^2\left(3\tilde{q}_0^2-2q_0^2\right), \qquad [9]\end{aligned}$$

as in the original PFC model with regular, even elasticity [where $\tilde{q}_0^2 = q_0^2$ and $\Gamma = 3A_0^2$ (45)]. The nonzero transverse interactions lead to additional elastic constants C_{iikl} ($k \neq l$) and C_{ijkk} ($i \neq j$), given by

$$\begin{aligned}C_{1112} &= C_{1121} = -\frac{1}{2}\Gamma A_0\tilde{q}_0^2\left(5\alpha_1-13\tilde{q}_0^2\alpha_2\right), \\ C_{2221} &= C_{2212} = -C_{1112} = -C_{1121}, \\ C_{1211} &= -C_{2122} = \frac{1}{2}\Gamma A_0\tilde{q}_0^2\left(7\alpha_1-23\tilde{q}_0^2\alpha_2\right), \\ C_{2111} &= -C_{1222} = \frac{3}{2}\Gamma A_0\tilde{q}_0^2\left(\alpha_1-\tilde{q}_0^2\alpha_2\right), \qquad [10]\end{aligned}$$

where the right mirror symmetry $C_{iikl} = C_{iilk}$ is still maintained due to global rotational invariance of the system and the lack of coupling to rotational degrees of freedom, while generally the left minor symmetry is broken, i.e., $C_{ijkk} \neq C_{jikk}$, as a result of nonzero internal torque caused by transverse interactions, which leads to $\sigma_{ij} \neq \sigma_{ji}$ (if $i \neq j$) and the breaking of angular momentum conservation. Notably, the major symmetry is no longer obeyed, with $C_{ijkk} \neq C_{kkij}$ and $C_{iikl} \neq C_{klii}$ in Eq. **10**, such that the system incorporates both even and odd elasticity, i.e.,

$$C_{iikl} = C_{iikl}^{(\text{e})} + C_{iikl}^{(\text{o})}, \qquad C_{ijkk} = C_{ijkk}^{(\text{e})} + C_{ijkk}^{(\text{o})}, \qquad [11]$$

consisting of even elasticity components $C_{ijkl}^{(\text{e})} = C_{klij}^{(\text{e})}$ satisfying major symmetry and odd elasticity components $C_{ijkl}^{(\text{o})} = -C_{klij}^{(\text{o})}$ which are antisymmetric and proportional to transverse interaction strength (with expressions determined by Eq. **10** and shown in *SI Appendix*). The bulk modulus B and shear modulus μ are then given by

$$\begin{aligned}B &= \frac{1}{2}\left(C_{1111}+C_{1122}\right) = 2\Gamma\tilde{q}_0^4, \\ \mu &= \frac{1}{2}\left(C_{1111}-C_{1122}\right) = \Gamma\tilde{q}_0^2\left(3\tilde{q}_0^2-2q_0^2\right). \qquad [12]\end{aligned}$$

Downloaded from https://www.pnas.org by UNIVERSITAETS DUESSELDORF on October 20, 2025 from IP address 134.99.64.130.

We can also identify the odd bulk modulus A induced by nonzero internal torque and the odd shear modulus K^o as

$$A = \frac{1}{2}\left(C_{2111} - C_{1211}\right) = -\Gamma A_0 \tilde{q}_0^2\left(\alpha_1 - 5\tilde{q}_0^2\alpha_2\right), \quad [13]$$

$$K^o = C_{1112} = -\frac{C_{2111} + C_{1211}}{2} = -\frac{\Gamma}{2}A_0\tilde{q}_0^2\left(5\alpha_1 - 13\tilde{q}_0^2\alpha_2\right).$$

All these are consistent with continuum odd elasticity theory (9), with elastic constants expressed explicitly in terms of T-PFC parameters.

Results and Discussion

Model Validation. In addition to the above analytic results which demonstrate that the T-PFC model developed here incorporates key aspects of the system symmetry (and symmetry breaking), chirality, and odd elastic properties, we have conducted numerical simulations to further validate the model, and to provide evidence for the multiscale nature of this approach where particle-scale resolution is still maintained in this continuum field description. Here, the T-PFC model Eq. **3** is solved numerically (*Materials and Methods*; see also *SI Appendix*), with the setting of $\alpha_2 = 0$ for a minimal continuum field model incorporating effects of transverse interaction and odd elasticity. (We have also conducted simulations with nonzero α_2 and found no significant differences.) Values of model parameters used in our simulations are summarized in *SI Appendix*, Table S1. In *SI Appendix*, we also present a procedure of model parameterization to match the model to experimental systems. We have reproduced various phenomena of odd and chiral crystals found in experiments and particle-based simulations and matched the results to the microscopic description based on interparticle forces, with some simulation outcomes illustrated in Fig. 1. These include self-rotation of odd crystallites (Fig. 1 *A* and *B* and Movie S1), as a result of nonzero net transverse force (or net odd stress) and thus a net torque on the free surface of a crystallite embedded in a homogeneous or liquid-state medium, consistent with experiments of, e.g., swimming bacteria (6), starfish embryos (7), and magnetic colloids (8) 2D chiral crystals. Also included are the behaviors of dislocation self-propulsion (Fig. 1*C*). A key phenomenon is the self-glide of a dislocation along the direction of its Burgers vector (Movie S2), which follows the direction of local net transverse force around the dislocation core as indicated in the schematic of Fig. 1*C*. For a dislocation dipole with opposite Burgers vectors and far enough separation, dislocation unbinding occurs (Movie S3), instead of annihilation in regular crystals (Movie S4). A circular grain boundary would either expand (Fig. 1*D* and Movie S5) or shrink (Movie S6), depending on the direction of Burgers vectors of boundary dislocations. These results of motile dislocation are consistent with those found in magnetic colloidal experiments and particle-based simulations (8, 10, 11), demonstrating that effects at microscopic, lattice scales (that are not accessible in standard continuum approaches) can be well captured in this continuum T-PFC model.

An advantage of PFC modeling is that it allows to simulate the process of dislocation climb, which is difficult to realize in atomistic simulations like MD as the dynamics involves long-range mass diffusion. As shown in Fig. 1*E*, two dislocations of opposite sign of Burgers vectors, which would climb toward each other and annihilate in regular crystals (Movie S7), travel apart due to self-gliding caused by transverse interaction (Movie S8). Note that in all the calculations presented here, we choose $\alpha_1 > 0$ which corresponds to the case of two-body transverse force along the direction $\hat{\mathbf{r}}_{ab}^{\perp} = \hat{\mathbf{z}} \times \hat{\mathbf{r}}_{ab}$. This leads to counterclockwise self-rotation of crystallites and the dislocation self-propulsion along the direction of Burgers vector, while choosing $\alpha_1 < 0$ with opposite direction of interparticle transverse force gives equivalent results, although with opposite direction of self-rotation (clockwise) and dislocation self-glide, as verified in our simulations.

We also quantitatively examine the property of self-rotation of single-crystalline grains, for which the grain rotates faster for larger transverse interaction strength α_1 and smaller grain size, consistent with the microscopic picture. Our T-PFC calculations of grain self-rotation frequency ω at different α_1 show the collapse of data into a power law scaling (Fig. 1*B*)

$$\frac{\omega}{\alpha_1} \sim N^{-s}, \quad [14]$$

with scaling exponent $s = 0.950 \pm 0.005$, where N is the number of particles in the grain. For comparison, we show in the *Inset* of Fig. 1*B* the data of the experimental measurement of rotating starfish embryo clusters (7) within the same range of N. Although the experimental data indicate a crossover between two regimes of ω scaling for small and large embryo number N, which might involve some biological mechanisms and could not be captured by our T-PFC continuum field modeling and by the related particle-based simulation (7), the overall trend of the ω variation is consistent with the scaling behavior identified in our modeling. To understand this N^{-1} scaling, consider the overdamped limit with $\zeta_R\omega = \tau_{\text{net}}$, where ζ_R is the rotational friction coefficient that can be estimated as $\zeta_R \propto R^4 \sim N^2$ for a 2D circular grain of radius R (*SI Appendix*), and the self-generated net torque on the grain surface $\tau_{\text{net}} = \int_s R\, dF_{\text{net}}^{\perp} \propto \oint R\alpha_1 ds \propto \alpha_1 R^2$ (if assuming balanced transverse interactions in the bulk). This leads to $\omega = \tau_{\text{net}}/\zeta_R \propto \alpha_1/R^2 \sim \alpha_1/N$.

Surface Cusp Instability and Grain Self-Fission. On the free surface of single-crystalline odd grains, the self-generated surface odd stress (with tangential, self-shearing surface net transverse force as illustrated in Fig. 1*A*) results in the spontaneous development of a surface cusp instability in the absence of any external strain or stress. An example with $\alpha_1 = 2$ is shown in the *Inset* of Fig. 2*A* and Movie S9. The subsequent nonlinear evolution leads to the nucleation of dislocations at the edges of surface cusps, which self-propel into the bulk as a result of the self-gliding of motile dislocation induced by transverse interaction (Fig. 2*B*). The instability occurs beyond a threshold of grain size, characterized by a critical radius R_c which is larger for weaker transverse interaction strength α_1. A scaling behavior of $R_c \sim |\alpha_1|^{-\beta}$ is identified from our numerical simulations (Fig. 2*A*), with a scaling exponent $\beta = 2.5 \pm 0.2$.

Note that the odd crystalline system studied here is nonpotential as a result of nonzero transverse interactions, and the system evolution governed by Eq. **3** does not follow the pathway of free energy minimization. Thus, this result of grain instability is of nonequilibrium, nonrelaxational nature and cannot be identified from energetics arguments used for near-equilibrium potential systems (see *SI Appendix* for a related calculation). The physical mechanism for this behavior of critical radius and scaling is governed by the competition between the destabilizing effect caused by the self-generated surface odd stress and the stabilizing effect of surface tension and can be understood through the mechanical force/stress condition on the surface. At a crystal-melt interface Σ, the mechanical force balance is given by (46)

$$\boldsymbol{\sigma} \cdot \hat{\mathbf{n}} + P_L\hat{\mathbf{n}} - \boldsymbol{\nabla}_{\Sigma} \cdot \boldsymbol{\sigma}_s = 0, \quad [15]$$

Downloaded from https://www.pnas.org by UNIVERSITAETS DUESSELDORF on October 20, 2025 from IP address 134.99.64.130.

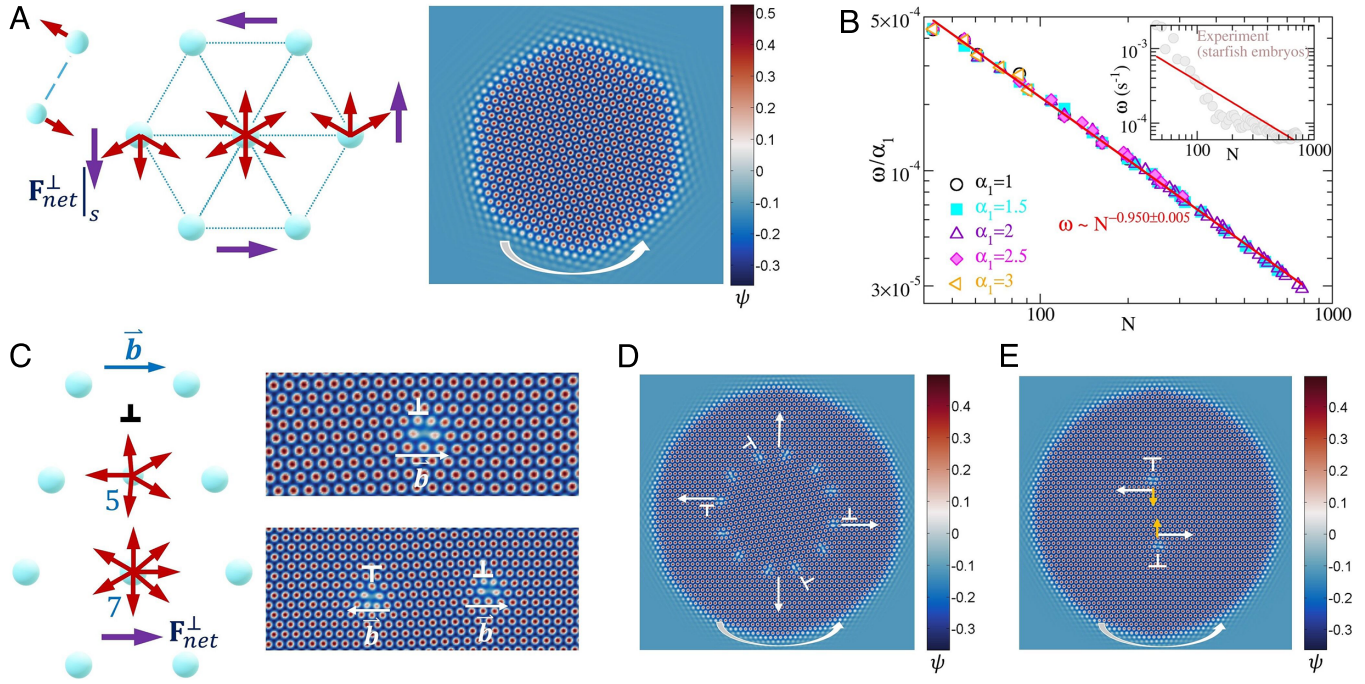

Fig. 1. T-PFC simulation results for self-rotating odd crystals and motile defects. (*A*) A snapshot of a self-rotating single-crystalline grain at $\alpha_1 = 2$, with a schematic illustrating nonzero net transverse force on the surface. (*B*) The scaling of grain rotation frequency ω vs. particle number N, showing a data collapse for different transverse interaction strength α_1. The *Inset* shows the experimental data of starfish-embryos living crystals in ref. 7 for the same N range. The simulation results are fitted into a power law scaling which is also indicated in the *Inset* for comparison. (*C*) Schematic of a penta-hepta dislocation with local nonzero net transverse force, which leads to dislocation self-glide and the unbinding of a dislocation dipole as shown in the snapshots of the simulated ψ profile. The Burgers vector **b** is labeled for each dislocation. (*D*) A self-expanding circular grain boundary within a self-rotating crystallite, with 8° misorientation at $\alpha_1 = 1$. (*E*) The climb and self-glide of two dislocations of opposite Burgers vectors at $\alpha_1 = 1$. Small arrows indicate the climb direction, and large arrows give the direction of self-glide along the Burgers vectors.

where $\hat{\mathbf{n}}$ is the surface unit normal, $\boldsymbol{\sigma}$ is the stress tensor of the crystallite, P_L is the pressure of the surrounding liquid or melt, $\boldsymbol{\nabla}_\Sigma$ represents the surface gradient, and $\boldsymbol{\sigma}_s$ is the surface stress tensor. For a steady-state 2D circular crystallite with radius R, $\hat{\mathbf{n}} = \hat{\mathbf{r}}$ with unit vector $\hat{\mathbf{r}}$ along the radial direction, $\boldsymbol{\nabla}_\Sigma \cdot \boldsymbol{\sigma}_s = -\sigma_s \kappa \hat{\mathbf{n}} = -(\sigma_s/R)\hat{\mathbf{r}}$ with surface curvature $\kappa = 1/R$, and $\boldsymbol{\sigma} \cdot \hat{\mathbf{n}}|_R = -P_S \hat{\mathbf{r}}$ for hydrostatic elastic bulk deformations, with no contribution from the net odd stress on the surface along the radial direction (Fig. 1*A*). We then have

$$P_S - P_L - \frac{\sigma_s}{R} = 0, \qquad [16]$$

which is the 2D solid-state analog of the Young–Laplace equation, but with surface energy replaced by surface stress σ_s (46–48). Now consider a small surface perturbation or deformation that leads to surface normal deviation from $\hat{\mathbf{r}}$, i.e., $\hat{\mathbf{n}} \to \hat{\mathbf{r}} + \delta\hat{\mathbf{n}}$. The odd stress $\boldsymbol{\sigma}^{(o)}$ should then give a nonzero contribution along the local surface normal at $r \approx R$, with $\boldsymbol{\sigma}^{(o)} \cdot \hat{\mathbf{n}}|_R \simeq \delta\sigma_R^{(o)} \delta\hat{\mathbf{n}}$, where the odd stress component on the surface, $\delta\sigma_R^{(o)}$, is proportional to transverse interaction strength α_1 and should weakly increase with smaller R due to a relatively stronger effect of deformation for smaller grain with a perturbed surface. This weak variation of $\delta\sigma_R^{(o)}$ would thus follow a sublinear decay over R, and we can expand in terms of a fractional power series [i.e., Puiseux series (49)] of $1/R$ with a small leading-order fractional exponent to account for this sublinear variation. Noting that R needs to be large enough for a nucleated solid grain to avoid being dissolved, it is hence a good approximation to keep the leading-order term of expansion which yields $\delta\sigma_R^{(o)} \simeq |\alpha_1| c_T (1/R)^\delta$, with a fractional exponent $0 < \delta < 1$ and a proportional constant c_T. The surface perturbation also leads to a modification of surface stress contribution, with $\boldsymbol{\nabla}_\Sigma \cdot \boldsymbol{\sigma}_s \simeq -\sigma_s \kappa \hat{\mathbf{n}} - \delta\sigma_s \kappa \delta\hat{\mathbf{n}}$. Making use of the mechanical force condition (Eq. **15**), we can then determine the surface perturbed velocity

$$\mathbf{v}_s \propto \left(\delta\sigma_R^{(o)} - \delta\sigma_s \kappa\right) \delta\hat{\mathbf{n}} \simeq \left(|\alpha_1| c_T R^{-\delta} - \frac{\delta\sigma_s}{R}\right) \delta\hat{\mathbf{n}}. \qquad [17]$$

The odd crystallite surface instability would occur when $\delta\sigma_R^{(o)} > \delta\sigma_s\kappa$ at $R > R_c$, resulting in a critical radius

$$R_c \propto |\alpha_1|^{-1/(1-\delta)}, \qquad [18]$$

and thus a scaling exponent $\beta = 1/(1-\delta)$. The above simulation result gives an exponent of $\beta \simeq 5/2$, indicating $\delta \simeq 3/5$. This is consistent with the assumption of small fractional δ for a sublinear variation of odd stress contribution on the perturbed surface.

At the later time stage of grain evolution, the continuing process of dislocation proliferation and self-traveling results in a recurring procedure of cracking and self-healing inside the rotating crystallite, yielding internal grain boundary formation and evolution as well as the overall grain distortion (see Movie S9 at $\alpha_1 = 2$). In the case of strong enough transverse interaction, it leads to the occurrence of grain self-fission with self-rotating fragments (Fig. 2*C* and Movie S10 at $\alpha_1 = 3$). Recent MD simulations and experiments of magnetic colloidal crystals (8) have observed the similar phenomenon of dislocation creation and propulsion from the free boundary of single-crystalline crystallite and the subsequent formation of multidomains and

Downloaded from https://www.pnas.org by UNIVERSITAETS DUESSELDORF on October 20, 2025 from IP address 134.99.64.130.

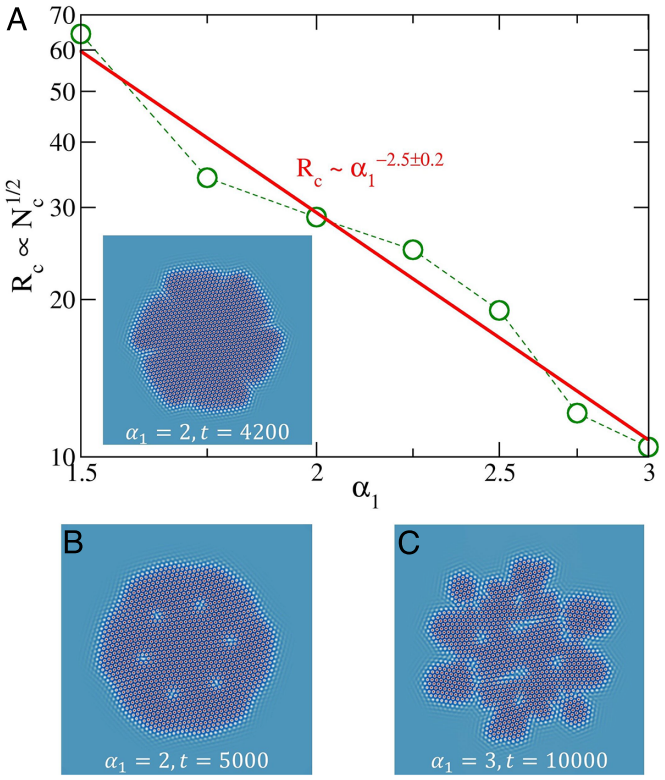

Fig. 2. (*A*) Critical grain radius R_c for the onset of surface cusp instability as a function of transverse interaction strength α_1, as identified from T-PFC simulations (up to $t = 10^6$). Snapshots of the ψ profile are shown in the *Inset* of (*A*) for the instability onset and in (*B*) for the surface-emitted motile dislocations at $\alpha_1 = 2$, and in (*C*) for grain self-fission at $\alpha_1 = 3$.

grain boundaries inside the crystallite, although the mechanism of cusp instability and its grain size dependence, as well as the self-division and the resulting grain distortion as found here, were not examined. Thus, the mechanism and results identified above are key to understanding those experimental findings. Note also that the phenomena of cusp instability and irregular grain self-fission obtained here for "dry" odd crystals originate from self-generated surface odd stresses resulting from transverse interactions, a mechanism that is intrinsically different from the self-shearing instability and flow-induced splitting of fluid droplets found in the "wet" system of Active Model H (50). Such a "wet" active model system is subjected to hydrodynamic flow coupling but not to transverse interactions (i.e., without any odd elastic or viscous properties), where the (not crystalline) fluid droplets form via phase separation and have negative surface tension caused by contractile active stress, leading to a self-shearing instability and droplet breaking. This mechanism of instability then differs fundamentally from the one described above for odd crystals, due to the lack of odd elasticity. The critical droplet size for the onset of instability and the corresponding scaling behavior, which have not been examined for this "wet" fluid system, are then expected to be qualitatively different as well.

Transition from Normal to Reverse Ostwald Ripening. This mechanism of self-stress induced surface instability and the resulting grain self-fission can lead to two phenomena of anomalous multigrain dynamics. The first one is the transition from normal Ostwald ripening to the reverse process with the increase of transverse interaction strength α_1, for two self-rotating odd crystalline grains. This is demonstrated in Fig. 3*A*, which shows the time evolution of grain sizes, defined as $L \simeq 2R = 2\sqrt{\mathcal{A}/\pi}$ with grain area $\mathcal{A}$, at α_1 ranging from 0 (for the original passive PFC model) to 3. The standard process of Ostwald ripening is observed at small enough magnitude of α_1 with zero or weak enough transverse interactions, as expected, for which the initially larger grain with effective radius $R_>(t)$ grows with time after an early time range of relaxation, accompanied by the shrinkage of the initially smaller grain with radius $R_<(t)$. At strong enough α_1, starting from the same initial conditions of grain sizes and spacing, reverse Ostwald ripening occurs when the initial radius $R_<(0)$ of the smaller grain is large enough, showing as the overall decrease of $R_>(t)$ with time and the early-time decrease, slowing-down, and then increase of $R_<(t)$ until both reach a similar scale (Fig. 3 *B* and *C*; see also Movie S11 (for $t \leq 20{,}000$) and Movie S12 (for $t = 95{,}000$ to 10^5), corresponding to the curves of $\alpha_1 = 3$ in Fig. 3*A*).

This transition can be explained by the behavior of grain self-division and fission. In the case of normal Ostwald ripening, according to the Gibbs–Thomson relation (51) [which has been generalized for the PFC model with the supersaturation of density variation field ψ (52)], i.e., $\delta\mu|_{\text{surface}} \propto \gamma\kappa$ with $\delta\mu = \mu - \mu_{\text{eq}}$, γ the surface tension, and κ the surface curvature, the chemical potential μ and thus particle density at the solid–liquid grain surface increase with the decreasing grain radius (i.e., larger κ), leading to a diffusive mass transport from smaller to larger grains as driven by the local density gradient and consequently, the growth of larger grain at the expense of shrinking and disappearance of smaller grain. This can be changed by strong enough transverse interactions. For a given initial radius $R_>$ of the larger self-rotating grain, when it exceeds the threshold size $R_c(\alpha_1)$, at a high enough α_1 (as quantified in Fig. 2*A*) a surface cusp instability and the subsequent dislocation proliferation, emission and grain self-fission occur, resulting in smaller fragmented subgrains and thus the reduced or even reversed local density gradient and diffusion flux with respect to the other grain (which has size $R_<$). This leads to the slowing-down, arrest, and reverse of the Ostwald ripening process with

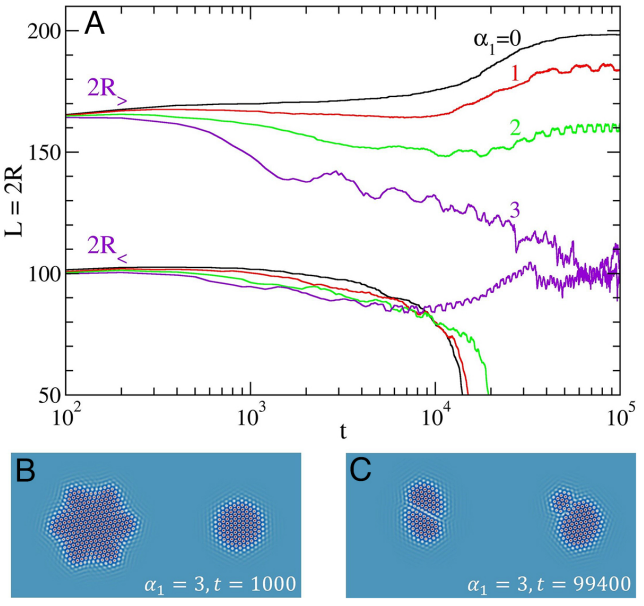

Fig. 3. (*A*) Time evolution of grain sizes during the ripening process of two crystalline grains, showing a transition from normal to reverse Ostwald ripening with the increase of α_1. (*B* and *C*) Simulation snapshots at $t = 1{,}000$ and 99,400 during the process of reverse Ostwald ripening with $\alpha_1 = 3$.

Downloaded from https://www.pnas.org by UNIVERSITAETS DUESSELDORF on October 20, 2025 from IP address 134.99.64.130.

the two grains approaching a similar, comparable size, as shown in Fig. 3 (for results of $\alpha_1 = 3$). At the late time stage when the radius of the initially smaller grain $R_<(t) > R_c$, grain self-fission also occurs there, in addition to the self-division of the other grain (Fig. 3*C* and Movie S12). On the other hand, if the initial $R_<(0)$ is too small, due to the Gibbs–Thomson effect, the smaller grain shrinks rapidly and melts before the self-fission and fragmentation of the larger grain take any effect.

This mechanism governing the reverse Ostwald ripening process for odd crystals is thus different from that of phase-separated active fluids caused by negative pseudotension of liquid droplet surface (50, 53), noting the increase of positive γ with stronger transverse interactions (which generate larger tangential surface stress) as found in simulations of chiral fluid interfaces (13). It is also different from the reverse ripening caused by misfit stress in passive solid systems (54), given the lack of any imposed stress or strain in the system studied here. Hence, the transition identified above is a unique feature combining chirality (breaking of 2D parity) and grain self-fission in this odd crystalline system.

Transition from Grain Coarsening to Grain Self-Fragmentation. The second phenomenon originating from the mechanism of surface cusp instability and grain self-fission is the spontaneous formation of a dynamical polycrystalline state during the nucleated growth process, where the system evolves from an initial condition of multiple randomly distributed crystalline nuclei. Examples of system time evolution at small and large α_1 are shown in Movies S13 ($\alpha_1 = 1$) and S14 ($\alpha_1 = 3$), with some simulation snapshots given in Fig. 4, both having the same average density $\bar{\psi}_0 = -0.09$ and starting from the same initial conditions. At the early time stage, a similar behavior is observed in both movies, including the fast growth of nuclei and the impingement and then coalescence of grains, but the subsequence evolution is qualitatively different. At small α_1 (weak transverse interactions), the system dynamics is governed by the motion of topological defects, particularly grain boundaries, similar to the typical process of grain coarsening, although with dislocation self-motion as a result of nonzero transverse force (Fig. 4*A* and Movie S13). However, for large α_1 (strong transverse interaction), any large enough self-rotating grains, formed after either grain growth or coalescence, exhibit self-fission into smaller parts through dislocation creation on grain surface and propagation across the grain with crack formation. Neighboring rotating grains then remerge or reheal, self-splitting again if exceeding the instability size threshold (R_c), with the procedure iterated incessantly. This leads to a persistently varying process of grain self-fragmentation instead of coarsening, as seen in Movie S14 and Fig. 4*B*.

To quantitatively examine this transition from the normal grain coarsening process to the anomalous dynamics of grain fragmentation, we calculate the structure factor $S(\mathbf{q}, t) = |\hat{\psi}_{\mathbf{q}}(t)|^2/V$, with $\hat{\psi}_{\mathbf{q}}(t)$ the Fourier transform of $\psi(\mathbf{r}, t)$ and

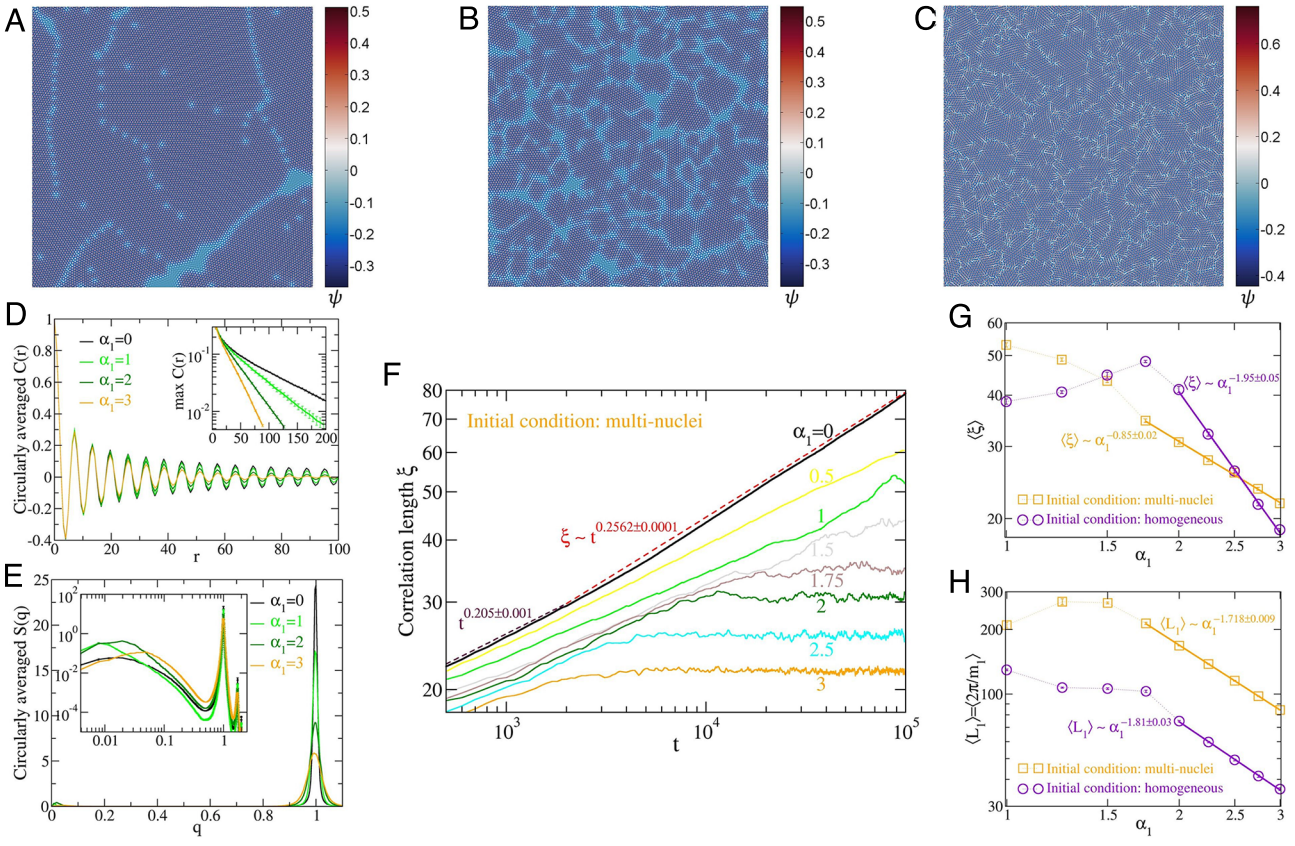

Fig. 4. Multigrain dynamics of the odd polycrystalline state. (*A–C*) Simulation snapshots at $t = 10^5$, each showing the central quarter of the 2,048 × 2,048 simulated system, for initial conditions of multiple crystalline nuclei with $\bar{\psi}_0 = -0.09$ at (*A*) $\alpha_1 = 1$ governed by grain coarsening dynamics and (*B*) $\alpha_1 = 3$ governed by grain self-fragmentation, and (*C*) from homogeneous initial state with $\bar{\psi}_0 = 0$ at $\alpha_1 = 3$. (*D*) Circularly averaged correlation function $C(r)$, with the *Inset* showing the exponential decay of its peak values, and (*E*) circularly averaged structure factor $S(q)$, with the corresponding log–log plots given in the *Inset*, both at $t = 10^5$ and for initial conditions of multiple nuclei. (*F*) Time variation of the correlation length ξ, showing a transition from grain coarsening to self-fragmentation dynamics with the increase of transverse interaction strength α_1. (*G* and *H*) $\langle\xi\rangle$ and $\langle L_1\rangle$, averaged over the late time stage ($t = 8 \times 10^4$ to 10^5), as a function of α_1, for two types of initial conditions. Power-law scalings are identified in the regime of grain self-fragmentation. Results in (*D–H*) have been averaged over 20 simulation runs for 2,048 × 2,048 system size.

Downloaded from https://www.pnas.org by UNIVERSITAETS DUESSELDORF on October 20, 2025 from IP address 134.99.64.130.

$V = L_x L_y$ for a 2D system of size $L_x \times L_y$, and the correlation function $C(\mathbf{r}, t) = (\langle \psi(\mathbf{x}+\mathbf{r}, t)\psi(\mathbf{x}, t)\rangle - \bar{\psi}_0^2)/(\langle \psi^2\rangle - \bar{\psi}_0^2)$ at different times t. The characteristic domain or grain size in the polycrystalline state is identified by two quantities, the correlation length $\xi(t)$ determined via the fitting of the envelope (or peak values) of circularly averaged correlation function to $C_m(r, t) \propto \exp(-r/\xi)$ (Fig. 4*D*), and domain size $L_1(t) = 2\pi/m_1$ where the first moment $m_1 = \int_0^{q_{m_1}} dq\, qS(q, t) / \int_0^{q_{m_1}} dq S(q, t)$ is evaluated within the first peak region of small wave numbers $0 < q \leq q_{m_1}$, with q_{m_1} the location of first local minimum of the circularly averaged structure factor $S(q, t)$ (see Fig. 4*E*, where the other peaks are located at the wave numbers of triangular lattice with ratios $1 : \sqrt{3} : 2$). Note that ξ measures the distance of correlation between local density fluctuations, giving the scale of domains separated by any defects or disorder, while L_1 characterizes the larger-scale profile of solid grains particularly those separated via locally homogeneous or liquid-like boundaries or gaps.

Results for the time evolution of the correlation length ξ are presented in Fig. 4*F*, clearly showing a transition from coarsening-dominated to fragmentation-dominated dynamics with the increase of transverse interaction strength α_1. A similar behavior is obtained for L_1 from calculations of the first moment. The self-fragmentation state appears earlier for stronger transverse interaction, as characterized by a fluctuating plateau of the average grain size which decreases with larger α_1 as a result of more dynamically fragmented grains. This is consistent with the α_1-dependence of threshold R_c for grain instability found in Fig. 2*A*, although with different values of the scaling exponent. The scalings of characteristic domain sizes averaged over a late time stage (e.g., $t = 8 \times 10^4$ to 10^5) are shown in Fig. 4 *G* and *H*, giving $\langle \xi \rangle \sim |\alpha_1|^{-\beta_\xi}$ and $\langle L_1 \rangle \sim |\alpha_1|^{-\beta_{m_1}}$ in the fragmentation-dominated regime, with scaling exponents $\beta_\xi = 0.85 \pm 0.02$ and $\beta_{m_1} = 1.718 \pm 0.009$, respectively (similar results are obtained if choosing different late time ranges for averaging or different system sizes). The transition point between regimes of two different grain dynamics can be estimated as the beginning of the scaling regime, which occurs around $\alpha_1 \simeq 1.75$ as identified from Fig. 4 *G* and *H*.

This phenomenon of multigrain self-fragmentation dynamics closely resembles the self-kneading polycrystal whorl state observed in recent experiments of magnetic colloidal odd crystals (8), where the average grain size is also found to decrease with stronger transverse interaction at higher colloid spinning frequency. This phenomenon, however, is fundamentally different from the clustering or rotating flocks observed in active chiral fluids composed of spinning colloidal particles (13, 55–57). There, although a steady state of finite size clusters without coarsening can form at high enough spinning rates, each of self-rotating clusters or flocks is in the liquid phase with the presence of edge current (13, 57) but without the mechanism of surface instability or grain self-fission found in the odd crystals studied here. Note that although the dynamical regime of grain fragmentation observed here involves the self-motion and flow or propagation of defects, intrinsically these defect self-flows still originate from the effects of transverse interactions and the associated odd stresses, while effects of hydrodynamic flow coupling by the liquid or melt surrounding the fragmented grains are not considered in this modeling and thus do not contribute to the properties identified above.

In the above study of multigrain dynamics, the average density of the system ($\bar{\psi}_0 = -0.09$) is chosen such that some small liquid-state regions or gaps can coexist with solid grains, facilitating the occurrence of grain surface instability. Our simulations indicate that the grain boundaries themselves, without any surrounding liquid, can also develop an instability and emit motile dislocations, causing self-fission of grains. We thus simulate systems of pure solid phase with high enough average density ($\bar{\psi}_0 = 0$), starting from initial conditions of spatially homogeneous phase. A polycrystalline state emerges spontaneously, with differently oriented domains separated by grain boundaries and dislocations. Similarly, the subsequent evolution is governed by two distinct types of dynamics, grain coarsening at weak transverse interaction strength α_1, and as α_1 increases, a transition to the persistent dynamical state of grain self-fragmentation (Movie S15 and Fig. 4*C*), although with a different morphology of self-rotating fragmented multigrains. Such a transition occurs at the similar magnitude of α_1, around $\alpha_1 \simeq 2$ as obtained from Fig. 4 *G* and *H*. It also features the power-law scalings of $\langle \xi \rangle$ and $\langle L_1 \rangle$, but with much larger exponents $\beta_\xi = 1.95 \pm 0.05$ and $\beta_{m_1} = 1.81 \pm 0.03$, indicating a more prominent effect of transverse interaction at high strength for the self-breaking of grains from grain boundaries.

We remark that the transition from grain coarsening to fragmentation is associated with a percolating network structure of grain boundaries, with an example shown in Fig. 4*C*. In contrast to defect networks in traditional material systems, the odd defect network emerging here becomes highly dynamical when transitioned to the grain fragmentation state, with network defect structures varying perpetually through the breaking of grain boundaries and grains self-fission and the subsequent remerging. This leads to a persistent process of breaking and restoring of the defect network connectivity, as seen in Movie S15 for a portion of the simulated system.

All the above results of transition from grain coarsening to self-fragmentation are robust as long as the system size is large enough such that individual grains or domains are able to exceed the size threshold to develop instability. At small α_1 for which the critical size R_c of grain instability could even reach or exceed the system size, the timescale for the development of instability is much longer than that of the coarsening process which would then dominate. Thus, the transition between the two regimes of multigrain dynamics is expected to be size independent for large systems, as verified in our simulations. We have simulated a larger system of size $4{,}096 \times 4{,}096$ (with five independent runs) for both types of initial conditions, and the results obtained, including the transition value of α_1 and scaling properties of characteristic domain sizes, are quantitatively very similar to those presented in Fig. 4 for a $2{,}048 \times 2{,}048$ system (with 20 runs).

Grain Locomotion. The surface effect induced by net transverse interaction can be utilized to control the locomotion of individual odd crystalline grains, showing as migration or transport of grains with directional self-motion (either translation or rotation) even though the constituent particles are not self-propelled. This is achieved by imposing spatially varying transverse interaction strengths $\alpha_{j=0,1,2}$ in the T-PFC Eq. **2**, which could correspond to spatial variation of individual particle spinning rates (as tuned by, e.g., rotating magnetic field applied to magnetic colloids, or similar avenues) that determine the magnitude of interparticle transverse force. It can be illustrated via an example of one-dimensional variation

$$\alpha_j(x) = \alpha_j^0 \cos Q_x(x - x_0), \qquad [19]$$

where $j = 0$, 1 and $Q_x = 2\pi/\lambda_x$ with λ_x the spatial periodicity of α_j variation which can be controlled by, e.g., spatial dependence

Downloaded from https://www.pnas.org by UNIVERSITAETS DUESSELDORF on October 20, 2025 from IP address 134.99.64.130.

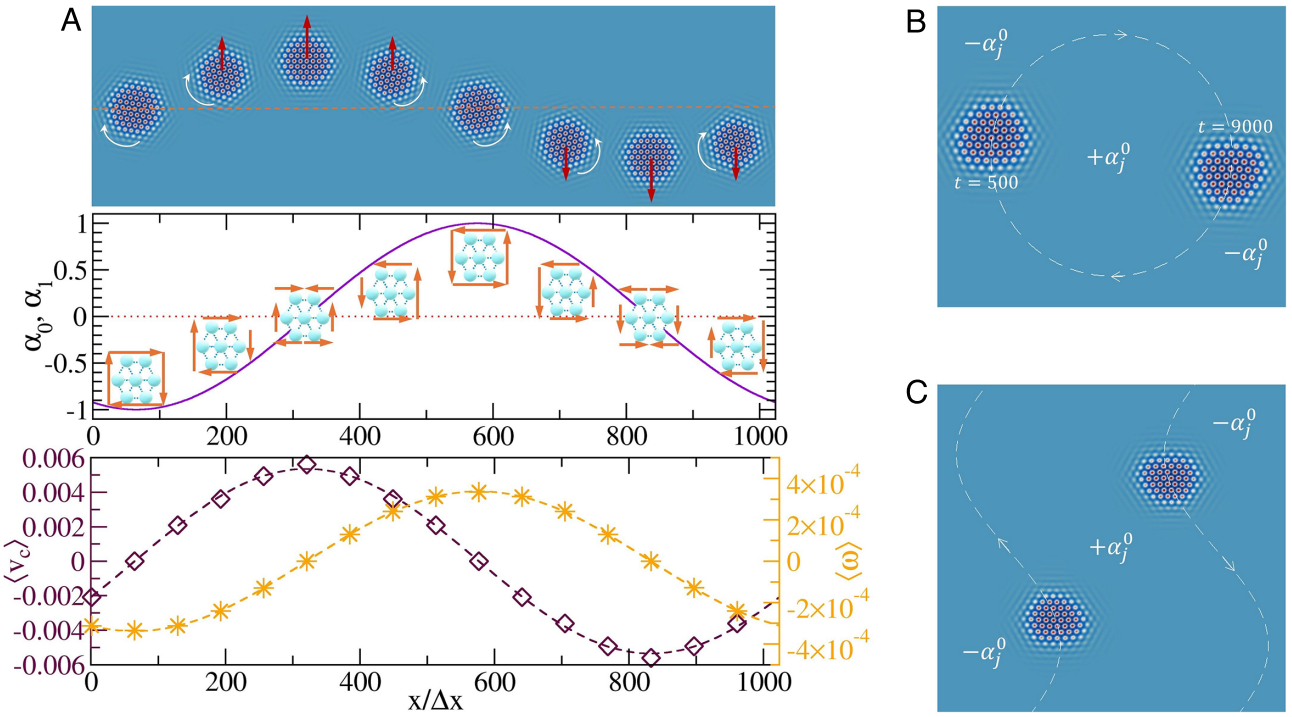

Fig. 5. Odd grain locomotion simulated via the T-PFC model. (*A*) A transition from self-rotation, self-rolling, to self-translation of grain locomotion as controlled via spatially varying transverse interaction strength $\alpha_0 = \alpha_1$. The rotational and translational directions of the grain are indicated as arrows in the *Top* panel which shows the simulation snapshot. The arrows in the *Middle* panel illustrate the net surface transverse forces for each grain, and the spatial dependence of self-translation velocity $\langle v_c \rangle$ and self-rotation frequency $\langle \omega \rangle$ (averaged over t = 3,000 to 5,000) is given in the *Bottom* panel, with dashed curves being the fitting to the data calculated from simulations. (*B* and *C*) The controlled transport of odd elastic grains along (*B*) a circular trajectory and (*C*) S-shaped tracks, through the predesigned 2D spatial distribution of $\alpha_{j=0,1}$.

of magnetic field for spinning magnetic particles. This leads to a continuous transition across different modes of grain locomotion, as demonstrated in Fig. 5*A* and Movie S16 (where $\alpha_0 = \alpha_1$ and $\alpha_2 = 0$). When located at the minimum (with $\alpha_{j=0,1} < 0$) and maximum (with $\alpha_{j=0,1} > 0$) of the spatially varying $\alpha_j(x)$, the grain self-rotates clockwise (CW) and counterclockwise (CCW), respectively, with the maximum magnitude of rotation frequency ω but with the absence of translational motion. In contrast, when the grain is centered at $\alpha_j = 0$ with antisymmetric distribution of $\alpha_{j=0,1}$ in its two sides, pure self-translation occurs, without any grain rotation, and the grain self-travels along a path perpendicular to the direction of α_j variation. In between these two limits of modes, the grain locomotes via the combination of self-rotating and self-translating, i.e., a behavior of self-rolling, and the directions of motion (CW vs. CCW rotation and $+y$ vs. $-y$ translation) depends on the type of asymmetric distribution of $\alpha_{j=0,1}$ around the grain.

This transition between different locomotion modes can be understood via the microscopic picture of the corresponding surface transverse forces, as illustrated by the schematics in the *Middle* panel of Fig. 5*A*. Note that nonzero net surface forces (or net surface odd stresses) are generated by the interparticle transverse interaction, as shown in the schematic of Fig. 1*A*. If the x-varying α_j distribution of transverse interaction strength is symmetric about the grain center, like the one located at the minimum of $\alpha_{j=0,1}$ (the leftmost schematic in the mid panel of Fig. 5*A*), the net surface tangential forces generated at the opposite x-sides and opposite y-sides of the grain are of equal magnitude but opposite direction; thus, there is no global translation force but a nonzero surface torque, leading to the behavior of pure self-rotation (CW in this case). When α_j increases, its asymmetric distribution along the x direction with respect to the grain center results in an unbalance of surface tangential forces on the opposite x-side surfaces, causing a nonzero global force pointed to the perpendicular y direction, together with the still nonzero but smaller net surface torque; this then leads to the behavior of self-rolling that combines $+y$ self-translation and slower CW self-rotation. A transition to the pure self-translation mode occurs when the grain center reaches $\alpha_j = 0$, for which α_j in the two x-sides are of opposite sign and distribute antisymmetrically, such that net forces on the two x-side surfaces are equal in terms of both magnitude and direction, giving maximum translational motion but zero surface torque (no rotation). Further increasing α_j into the positive regime leads again to the unbalanced surface forces but CCW self-rotation, back to the phenomenon of self-rolling, until reaching the maximum location of α_j with its symmetric distribution across the grain and hence pure CCW self-rotation. The other half period of α_j variation follows the same microscopic mechanism, giving the self-traveling along the $-y$ direction and the variation from CCW to CW self-rotation, as seen in Fig. 5*A* and Movie S16.

As also shown in Fig. 5*A*, the time-average self-translation velocity $\langle v_c \rangle$ calculated at the steady state of simulations, with v_c the velocity of centroid (geometric center) of the grain, is well fitted to a form $\langle v_c \rangle = v_{c0} \sin Q_x(x - x_0)$, while the self-rotation frequency obeys $\langle \omega \rangle = \omega_0 \cos Q_x(x - x_0)$, with $\omega > 0$ for CCW rotation and $\omega < 0$ for CW rotation, in phase with the α_j variation if compared to Eq. **19**. This indicates a $\pi/2$ phase difference between grain self-translation and self-rotation, consistent with the above microscopic picture. It is noted that the behaviors of grain locomotion identified here are characterized

Downloaded from https://www.pnas.org by UNIVERSITAETS DUESSELDORF on October 20, 2025 from IP address 134.99.64.130.

by rigid-body self-motion of odd elastic crystallites, different from the usual scenarios of locomotion accompanied by body shape changes as being implemented recently in the adaptive locomotion of active metamaterials with odd elastic responses (58).

Note that to obtain the above results of locomotion and mode transition, we have utilized the spatial modulation of $\alpha_1(\mathbf{r})$, in addition to that of the lowest-gradient α_0 term. Our elasticity analysis given above (and in *SI Appendix*) shows that the α_0 term itself does not generate odd elasticity, and thus the corresponding effect of grain self-rotation would not be expected. This has been verified in our simulations, where we use the same setup as that of Fig. 5*A* other than choosing $\alpha_0^0 = 1$ and $\alpha_1^0 = 0$ in Eq. **19** (instead of $\alpha_0^0 = \alpha_1^0 = 1$ in Fig. 5). Only grain self-translation is observed, but not self-rotation. Also, the grain becomes immobile at the smoothly varying peak and valley locations of $\alpha_0(\mathbf{r})$, as expected from the corresponding very small value of the $\boldsymbol{\nabla}(\alpha_0\psi) \times \boldsymbol{\nabla}\psi$ term in Eq. **2** which then makes a negligible contribution to the grain self-motion. Thus, maintaining the α_1 term is important to ensure effects of odd elasticity and achieve the control of transition between different locomotion modes.

These results and the mechanism unveiled enable us to steer the locomotion or transport of grains along the desired paths. This can be achieved via the predesigned 2D spatial distribution of transverse interaction strengths. Some simulation outcomes are presented in Fig. 5 *B* and *C* and Movies S17 and S18, for two examples of circular and S-shaped tracks for controlled locomotion. Here, we approximate a kink-type α_j profile separating inner (with $\alpha_j = \alpha_j^{\text{in}}$) and outer (with $\alpha_j = \alpha_j^{\text{out}}$) domains as

$$\alpha_j(\mathbf{r}) = \frac{1}{2}\left(\alpha_j^{\text{out}} + \alpha_j^{\text{in}}\right) + \frac{1}{2}\left(\alpha_j^{\text{out}} - \alpha_j^{\text{in}}\right)\tanh\left(\frac{R_s(\mathbf{r})}{\Delta}\right), \quad [20]$$

where $R_s(\mathbf{r})$ is the signed distance function from position $\mathbf{r}$ to the domain boundary (i.e., the boundary track for grain motion; see *Materials and Methods*) and Δ controls the boundary width. For simplicity, we set $\alpha_j^{\text{in}} = -\alpha_j^{\text{out}} \equiv \alpha_j^0$, such that $\alpha_j = 0$ at the positions of boundary. When initialized with the grain center located at the boundary track, with $+/-$ antisymmetric α_j distribution across the boundary, the grain will self-travel by following the exact track that has been predesigned, as seen in Fig. 5 and Movies S17 and S18. The direction of grain translation is always perpendicular to the local variation direction (i.e., spatial gradient) of transverse interaction strength α_j, based on the mechanism described above and illustrated in Fig. 5*A*. The maneuver of locomotion modes can be expected also from Fig. 5*A*, by placing the grain at an initial location deviated from the domain boundary, subjected to asymmetric distribution of α_j; the grain will then locomote via self-rolling, as verified in our simulations.

Conclusions and Outlook

We have developed a multiscale density field theory, the T-PFC model incorporating microscopic and mesoscopic length scales and diffusive timescales, for the study of complex dynamical behaviors of 2D chiral crystalline systems that are governed by both longitudinal and transverse interactions. The model incorporates nonreciprocity, 2D parity symmetry breaking, and odd elasticity through lowest-order field-theoretical terms originating from transverse interactions. This nonpotential continuum-field model is validated by the study of odd crystallite self-rotation, dislocation self-motion, unbinding of dislocation dipoles instead of annihilation, and motion of grain boundaries, with results well agreeing with those observed in recent experiments and particle-based simulations of various systems formed by, e.g., starfish embryos, magnetic colloids, and swimming bacteria, and consistent with the microscopic picture of transverse forces.

Importantly, this modeling unveils a distinct type of surface cusp instability, which is the precursor of the subsequent surface dislocation nucleation and proliferation as well as the occurrence of self-fission or self-division of single-crystalline grains for strong enough transverse interaction. This behavior of grain self-fission leads to the prediction of a transition from normal to reverse Ostwald ripening and the spontaneous formation of a dynamical polycrystalline state with its governing dynamics transitioning from the normal grain coarsening to the persistently varying process of grain self-fragmentation as effects of transverse interaction become more prominent. The critical radius of grain instability and the characteristic grain sizes in the fragmentation-dominated regimes are found to obey power-law scaling behaviors with respect to the transverse interaction strength. Also achieved is grain locomotion without shape changes as effected by net transverse interactions on grain surface, with transition between different modes of self-rotating, self-rolling, and self-translating that are controlled via local spatial variation of transverse interaction strengths. The corresponding mechanism can be used to steer the transport of individual odd grain along designed trajectories that are either straight or curved, an intriguing feature for odd elastic systems.

The T-PFC model developed here constitutes a bridging between particle-based microscopic picture and continuum odd elasticity theory, enabling the simulations across a broad range of scales and system sizes that are of experimental relevance (ranging from a few to tens of thousands of particles), as demonstrated in the above calculations. Much larger systems can be simulated when needed, without losing particle resolution, through this T-PFC modeling and also the corresponding mesoscopic amplitude equations (Eqs. **5** and **6**) as has been well demonstrated in previous PFC studies of passive systems. The modeling can be applied to examine and predict much more complex phenomena in chiral, odd crystalline systems that are beyond those presented here, such as mechanical and dynamical properties subjected to various external conditions, plastic deformation and dynamics of topological defects under variations of transverse interaction strengths, effects of confinements with different geometries and topologies, among many others. An interesting application for models of this type would be magnetic skyrmions, another example for a system with transverse interactions (59–61) and in particular odd elasticity (10). In addition, the model is readily extended to the study of self-propelled spinners (62) and multicomponent mixtures with transverse interactions within the same and between different species, which are expected to generate a rich variety of complex dynamical behaviors and patterns as a result of coupling and competition between different degrees of freedom and multiple scales that can be well described by this PFC-type continuum approach.

Materials and Methods

Numerical Simulations. The T-PFC model Eqs. **2** or **3** is solved numerically via the pseudospectral method with the use of periodic boundary conditions. A corresponding code is available in a GitHub repository (63). The model parameters are chosen as $\epsilon = 0.1$, $g = 0.5$, $q_0 = 1$, and $\alpha_2 = 0$, with different values of α_1 and average density $\bar{\psi}_0$. When studying the cases with solid–liquid coexistence, $\bar{\psi}_0$ values in solid and liquid regions are chosen and adjusted according to the phase diagram calculated from original PFC (26)

Downloaded from https://www.pnas.org by UNIVERSITAETS DUESSELDORF on October 20, 2025 from IP address 134.99.64.130.

given that in one-mode approximation effects of transverse interaction can be neglected in the perfect bulk state. Sizes of simulated systems range from 512×512 to $4{,}096 \times 4{,}096$ grid points, with grid spacing $\Delta x = \Delta y = \pi/4$ and simulation time step $\Delta t = 0.5$ (with similar results obtained if using smaller Δt). Thus, each system simulated for the study of multigrain dynamics in the polycrystalline state shown in Fig. 4 (of size $2{,}048 \times 2{,}048$ up to $t = 10^5$) contains roughly 10^5 particles or density peaks. More details of simulation setups are given in *SI Appendix*.

For the study of grain locomotion, the simulated system size is set as $1{,}024 \times 512$ grid points in Fig. 5*A* (with $\bar{\psi}_0|_{\text{solid}} = -0.076$ and $\bar{\psi}_0|_{\text{liquid}} = -0.116$) and 512×512 in Fig. 5 *B* and *C* (with $\bar{\psi}_0|_{\text{solid}} = -0.078$ and $\bar{\psi}_0|_{\text{liquid}} = -0.115$). The parameters used for the setup of α_j spatial variations are $\alpha_0^0 = \alpha_1^0 = 1$, $Q_x = 2\pi/L_x$ with $L_x = 1{,}024\Delta x$, $x_0 = 9L_x/16$, and $\Delta = 8\Delta x$. For the circular trajectory shown in Fig. 5*B*, the signed distance function R_s in Eq. **20** of the corresponding $\alpha_j(\mathbf{r})$ profile is given by

$$R_s(\mathbf{r}) = |\mathbf{r} - \mathbf{r}_c| - r_0, \qquad [21]$$

with center position $\mathbf{r}_c$ and radius r_0 of the circle. For the S-shaped channel with two boundary tracks shown in Fig. 5*C*, the corresponding R_s in Eq. **20** is approximated by

$$R_s(\mathbf{r}) \approx |x - x_c| - [r_0 \mp S_0 \sin(Q_s(y - y_c))], \qquad [22]$$

where (x_c, y_c) is the location of the channel center, r_0 is the half width of the channel, S_0 and Q_s give the amplitude and wave number of the periodic S-shaped modulation, and "$-$" ("$+$") is used for the region of $x > x_c$ ($x < x_c$). A variety of other types of α_j spatial profiles, with the corresponding boundary tracks set for different geometries or topologies, can be set up in a similar way through $R_s(\mathbf{r})$ (see, e.g., ref. 40).

Data, Materials, and Software Availability. Code data have been deposited in GitHub (https://doi.org/10.5281/zenodo.16790022) (63). All other data are included in the manuscript and/or supporting information.

ACKNOWLEDGMENTS. We thank Tzer Han Tan for providing the experimental data for cluster rotation frequencies of starfish embryos. Z.-F.H. acknowledges the support from the NSF under Grant No. DMR-2006446. M.t.V., R.W., and H.L. are funded by the Deutsche Forschungsgemeinschaft (DFG, German Research Foundation)–Project-IDs 465145163–SFB 1552 (M.t.V.), 535275785 (R.W.), and LO 418/29-1 (H.L.).

Author affiliations: [a]Department of Physics and Astronomy, Wayne State University, Detroit, MI 48201; [b]Institut für Physik, Johannes Gutenberg-Universität Mainz, 55128 Mainz, Germany; [c]Department of Physics, RWTH Aachen University, 52074 Aachen, Germany; [d]DWI - Leibniz Institute for Interactive Materials, 52074 Aachen, Germany; and [e]Institut für Theoretische Physik II: Weiche Materie, Heinrich-Heine-Universität Düsseldorf, 40225 Düsseldorf, Germany

1. L. Ratke, P. W. Voorhees, *Growth and Coarsening: Ostwald Ripening in Material Processing* (Springer, Berlin, 2002).
2. J. W. Cahn, J. E. Taylor, A unified approach to motion of grain boundaries, relative tangential translation along grain boundaries, and grain rotation. *Acta Mater.* **52**, 4887–4898 (2004).
3. C. Qiu *et al*., Grain boundaries are Brownian ratchets. *Science* **385**, 980–985 (2024).
4. M. Leoni, T. B. Liverpool, Dynamics and interactions of active rotors. *EPL* **92**, 64004 (2011).
5. Y. Fily, A. Baskaran, M. C. Marchetti, Cooperative self-propulsion of active and passive rotors. *Soft Matter* **8**, 3002–3009 (2012).
6. A. P. Petroff, X. L. Wu, A. Libchaber, Fast-moving bacteria self-organize into active two-dimensional crystals of rotating cells. *Phys. Rev. Lett.* **114**, 158102 (2015).
7. T. H. Tan *et al*., Odd dynamics of living chiral crystals. *Nature* **607**, 287–293 (2022).
8. E. S. Bililign *et al*., Motile dislocations knead odd crystals into whorls. *Nat. Phys.* **18**, 212–218 (2022).
9. C. Scheibner *et al*., Odd elasticity. *Nat. Phys.* **16**, 475–480 (2020).
10. L. Braverman, C. Scheibner, B. VanSaders, V. Vitelli, Topological defects in solids with odd elasticity. *Phys. Rev. Lett.* **127**, 268001 (2021).
11. A. Poncet, D. Bartolo, When soft crystals defy Newton's third law: Nonreciprocal mechanics and dislocation motility. *Phys. Rev. Lett.* **128**, 048002 (2022).
12. S. H. Choi, Z.-F. Huang, N. Goldenfeld, Noise-driven odd elastic waves in living chiral active matter. arXiv [Preprint] (2024). http://arxiv.org/abs/2411.09615.
13. C. B. Caporusso, G. Gonnella, D. Levis, Phase coexistence and edge currents in the chiral Lennard-Jones fluid. *Phys. Rev. Lett.* **132**, 168201 (2024).
14. L. Caprini, U. Marini Bettolo Marconi, Bubble phase induced by odd interactions in chiral systems. *J. Chem. Phys.* **162**, 161101 (2025).
15. S. Shankar, L. Mahadevan, Active hydraulics and odd elasticity of muscle fibres. *Nat. Phys.* **20**, 1501–1508 (2024).
16. M. J. Bowick, N. Fakhri, M. C. Marchetti, S. Ramaswamy, Symmetry, thermodynamics, and topology in active matter. *Phys. Rev. X* **12**, 010501 (2022).
17. Z. You, A. Baskaran, M. C. Marchetti, Nonreciprocity as a generic route to traveling states. *Proc. Natl. Acad. Sci. U.S.A.* **117**, 19767–19772 (2020).
18. F. Brauns, M. C. Marchetti, Nonreciprocal pattern formation of conserved fields. *Phys. Rev. X* **14**, 021014 (2024).
19. S. Saha, J. Agudo-Canalejo, R. Golestanian, Scalar active mixtures: The nonreciprocal Cahn-Hilliard model. *Phys. Rev. X* **10**, 041009 (2020).
20. G. Pisegna, S. Saha, R. Golestanian, Emergent polar order in nonpolar mixtures with nonreciprocal interactions. *Proc. Natl. Acad. Sci. U.S.A.* **121**, e2407705121 (2024).
21. D. Greve, G. Lovato, T. Frohoff-Hülsmann, U. Thiele, Coexistence of uniform and oscillatory states resulting from nonreciprocity and conservation laws. *Phys. Rev. Lett.* **134**, 018303 (2025).
22. Z.-F. Huang, M. te Vrugt, R. Wittkowski, H. Löwen, Active pattern formation emergent from single-species nonreciprocity. arXiv [Preprint] (2024). http://arxiv.org/abs/2404.10093.
23. S. J. Kole *et al*., Non-reciprocal interactions drive emergent chiral crystallites. arXiv [Preprint] (2025). http://arxiv.org/abs/2501.15996.
24. K. R. Elder, M. Katakowski, M. Haataja, M. Grant, Modeling elasticity in crystal growth. *Phys. Rev. Lett.* **88**, 245701 (2002).
25. K. R. Elder, N. Provatas, J. Berry, P. Stefanovic, M. Grant, Phase field crystal modeling and classical density functional theory of freezing. *Phys. Rev. B* **75**, 064107 (2007).
26. N. Provatas, K. R. Elder, *Phase Field Methods in Materials Science and Engineering* (Wiley-VCH, Weinheim, 2010).
27. P. Y. Chan, N. Goldenfeld, J. Dantzig, Molecular dynamics on diffusive time scales from the phase-field-crystal equation. *Phys. Rev. E* **79**, 035701 (2009).
28. S. K. Mkhonta, K. R. Elder, Z.-F. Huang, Exploring the complex world of two-dimensional ordering with three modes. *Phys. Rev. Lett.* **111**, 035501 (2013).
29. Z.-L. Wang, Z. R. Liu, Z.-F. Huang, Angle-adjustable density field formulation for the modeling of crystalline microstructure. *Phys. Rev. B* **97**, 180102 (2018).
30. M. Salvalaglio, K. R. Elder, Coarse-grained modeling of crystals by the amplitude expansion of the phase-field crystal model: An overview. *Model. Simul. Mater. Sci. Eng.* **30**, 053001 (2022).
31. H. Emmerich *et al*., Phase-field-crystal models for condensed matter dynamics on atomic length and diffusive time scales: An overview. *Adv. Phys.* **61**, 665–743 (2012).
32. A. Adland, Y. Xu, A. Karma, Unified theoretical framework for polycrystalline pattern evolution. *Phys. Rev. Lett.* **110**, 265504 (2013).
33. R. Backofen, K. Barmak, K. R. Elder, A. Voigt, Capturing the complex physics behind universal grain size distributions in thin metallic films. *Acta Mater.* **64**, 72–77 (2014).
34. K. A. Moats, E. Asadi, M. Laradji, Phase field crystal simulations of the kinetics of Ostwald ripening in two dimensions. *Phys. Rev. E* **99**, 012803 (2019).
35. M. Salvalaglio *et al*., A coarse-grained phase-field crystal model of plastic motion. *J. Mech. Phys. Solids* **137**, 103856 (2020).
36. M. W. Liu, M. P. Gururajan, K. A. Wu, Morphological evolution of grain boundaries under lateral strains. *Phys. Rev. Mater.* **6**, 023601 (2022).
37. D. Burns, N. Provatas, M. Grant, Two dimensional phase field crystal study of thermo-density coupling: Thermal expansion, recalescence, and plasticity. *Acta Mater.* **267**, 119712 (2024).
38. A. M. Menzel, H. Löwen, Traveling and resting crystals in active systems. *Phys. Rev. Lett.* **110**, 055702 (2013).
39. Z.-F. Huang, A. M. Menzel, H. Löwen, Dynamical crystallites of active chiral particles. *Phys. Rev. Lett.* **125**, 218002 (2020).
40. Z.-F. Huang, H. Löwen, A. Voigt, Defect dynamics in active smectics induced by confining geometry and topology. *Commun. Phys.* **5**, 294 (2022).
41. M. P. Holl, A. B. Steinberg, U. Thiele, Motility-induced crystallization and rotating crystallites. arXiv [Preprint] (2024). http://arxiv.org/abs/2408.06114.
42. Z.-F. Huang, K. R. Elder, N. Provatas, Phase-field-crystal dynamics for binary systems: Derivation from dynamical density functional theory, amplitude equation formalism, and applications to alloy heterostructures. *Phys. Rev. E* **82**, 021605 (2010).
43. J. Bickmann, S. Bröker, J. Jeggle, R. Wittkowski, Analytical approach to chiral active systems: Suppressed phase separation of interacting Brownian circle swimmers. *J. Chem. Phys.* **156**, 194904 (2022).
44. N. Goldenfeld, B. P. Athreya, J. A. Dantzig, Renormalization group approach to multiscale simulation of polycrystalline materials using the phase field crystal model. *Phys. Rev. E* **72**, 020601 (2005).
45. K. R. Elder, Z.-F. Huang, N. Provatas, Amplitude expansion of the binary phase-field-crystal model. *Phys. Rev. E* **81**, 011602 (2010).
46. P. H. Leo, R. F. Sekerka, The effect of surface stress on crystal-melt and crystal-crystal equilibrium. *Acta Metall.* **37**, 3119–3138 (1989).
47. J. W. Cahn, Surface stress and the chemical equilibrium of small crystals - I. The case of the isotropic surface. *Acta Metall.* **28**, 1333–1338 (1980).
48. W. W. Mullins, Thermodynamic equilibrium of a crystalline sphere in a fluid. *J. Chem. Phys.* **81**, 1436–1442 (1984).
49. V. Puiseux, Nouvelles recherches sur les fonctions algébriques. *J. Math. Pures Appl.* **16**, 228–240 (1851).
50. R. Singh, M. E. Cates, Hydrodynamically interrupted droplet growth in scalar active matter. *Phys. Rev. Lett.* **123**, 148005 (2019).
51. J. S. Langer, Instabilities and pattern-formation in crystal growth. *Rev. Mod. Phys.* **52**, 1–28 (1980).
52. Z.-F. Huang, Scale-coupling and interface-pinning effects in the phase-field-crystal model. *Phys. Rev. E* **87**, 012401 (2013).
53. E. Tjhung, C. Nardini, M. E. Cates, Cluster phases and bubbly phase separation in active fluids: Reversal of the Ostwald process. *Phys. Rev. X* **8**, 031080 (2018).

Downloaded from https://www.pnas.org by UNIVERSITAETS DUESSELDORF on October 20, 2025 from IP address 134.99.64.130.

54. C. H. Su, P. W. Voorhees, The dynamics of precipitate evolution in elastically stressed solids - I. Inverse coarsening. *Acta Mater.* **44**, 1987–1999 (1996).
55. B. Liebchen, D. Levis, Collective behavior of chiral active matter: Pattern formation and enhanced flocking. *Phys. Rev. Lett.* **119**, 058002 (2017).
56. B. Zhang, A. Sokolov, A. Snezhko, Reconfigurable emergent patterns in active chiral fluids. *Nat. Commun* **11**, 4401 (2020).
57. H. Massana-Cid, D. Levis, R. J. H. Hernández, I. Pagonabarraga, P. Tierno, Arrested phase separation in chiral fluids of colloidal spinners. *Phys. Rev. Res.* **3**, L042021 (2021).
58. J. Veenstra *et al*., Adaptive locomotion of active solids. *Nature* **639**, 935–941 (2025).
59. E. Kalz, H. D. Vuijk, J. U. Sommer, R. Metzler, A. Sharma, Oscillatory force autocorrelations in equilibrium odd-diffusive systems. *Phys. Rev. Lett.* **132**, 057102 (2024).
60. C. Reichhardt, C. J. O. Reichhardt, M. V. Milošević, Statics and dynamics of skyrmions interacting with disorder and nanostructures. *Rev. Mod. Phys.* **94**, 035005 (2022).
61. K. Everschor-Sitte, J. Masell, R. M. Reeve, M. Kläui, Perspective: Magnetic skyrmions-overview of recent progress in an active research field. *J. Appl. Phys.* **124**, 240901 (2018).
62. P. Chen *et al*., Self-propulsion, flocking and chiral active phases from particles spinning at intermediate Reynolds numbers. *Nat. Phys.* **21**, 146–154 (2025).
63. Z.-F. Huang, A Fortran code for numerically solving the T-PFC model equation. Zenodo. https://doi.org/10.5281/zenodo.16790022. Deposited 10 August 2025.

Downloaded from https://www.pnas.org by UNIVERSITAETS DUESSELDORF on October 20, 2025 from IP address 134.99.64.130.